Journal of Nanobiotechnology

RESEARCH

Open Access

Renal-clearable and tumor-retained nanodots overcoming metabolic reprogramming to boost mitochondrial-targeted photodynamic therapy in triple-negative breast cancer

Defan Yao[1,2†], Yanshu Wang[1†], Xue Dong[1†], Yanhong Chen[1], Ding-Kun Ji[3], Rongfeng Zou[4], Yuelin Huang[1], Weixi Huang[1] and Dengbin Wang[1,2*]

Abstract

Background Targeting tumor metabolism reprogramming has demonstrated a synergistic antitumor effect in photodynamic therapy of triple-negative breast cancer (TNBC). However, such a combination therapeutic regimen has encountered challenges, such as limited photosensitizer bioavailability and severe drug toxicity.

Methods and results Herein, ultrasmall metal-organic frameworks (MOFs) nanodots (MSPC) that encapsulate metabolism inhibitors and mitochondria-targeted photosensitizers are designed and fabricated for synergistic photodynamic therapy (PDT) of TNBC. The MSPC exhibits an acidic-sensitive drug release, leading to glutathione depletion and mitochondrial respiration suppression. Significantly, MSPC substantially reduces intracellular adenosine triphosphate (ATP) levels by simultaneously disrupting oxidative phosphorylation and impeding aerobic glycolysis. Therefore, the glutathione depletion combined with metabolism inhibitor increases oxidative stress, which improves the efficacy of mitochondria-targeted PDT. Additionally, the increased retention of photosensitizers within tumors, facilitated by aggregation-enhanced retention (AER) effect, extends the time window for long-term fluorescence/photoacoustic imaging-guided PDT of TNBC. MSPC-sensitized PDT significantly suppresses tumor growth with a single-dose injection and repeatable PDT.

Conclusions In summary, these renal-clearable and aggregation-enhanced tumor-retained nanodots indicate the feasibility of overcoming resistance to reactive oxygen species induced by metabolic reprogramming, thus holding significant implications for boosting PDT of TNBC.

†Defan Yao, Yanshu Wang and Xue Dong contributed equally to this work.

*Correspondence:
Dengbin Wang
wangdengbin@xinhuamed.com.cn

Full list of author information is available at the end of the article

Keywords Aggregates, Tumor microenvironment, Photodynamic therapy, Metal-organic frameworks, Triple-negative breast cancer

Graphical Abstract

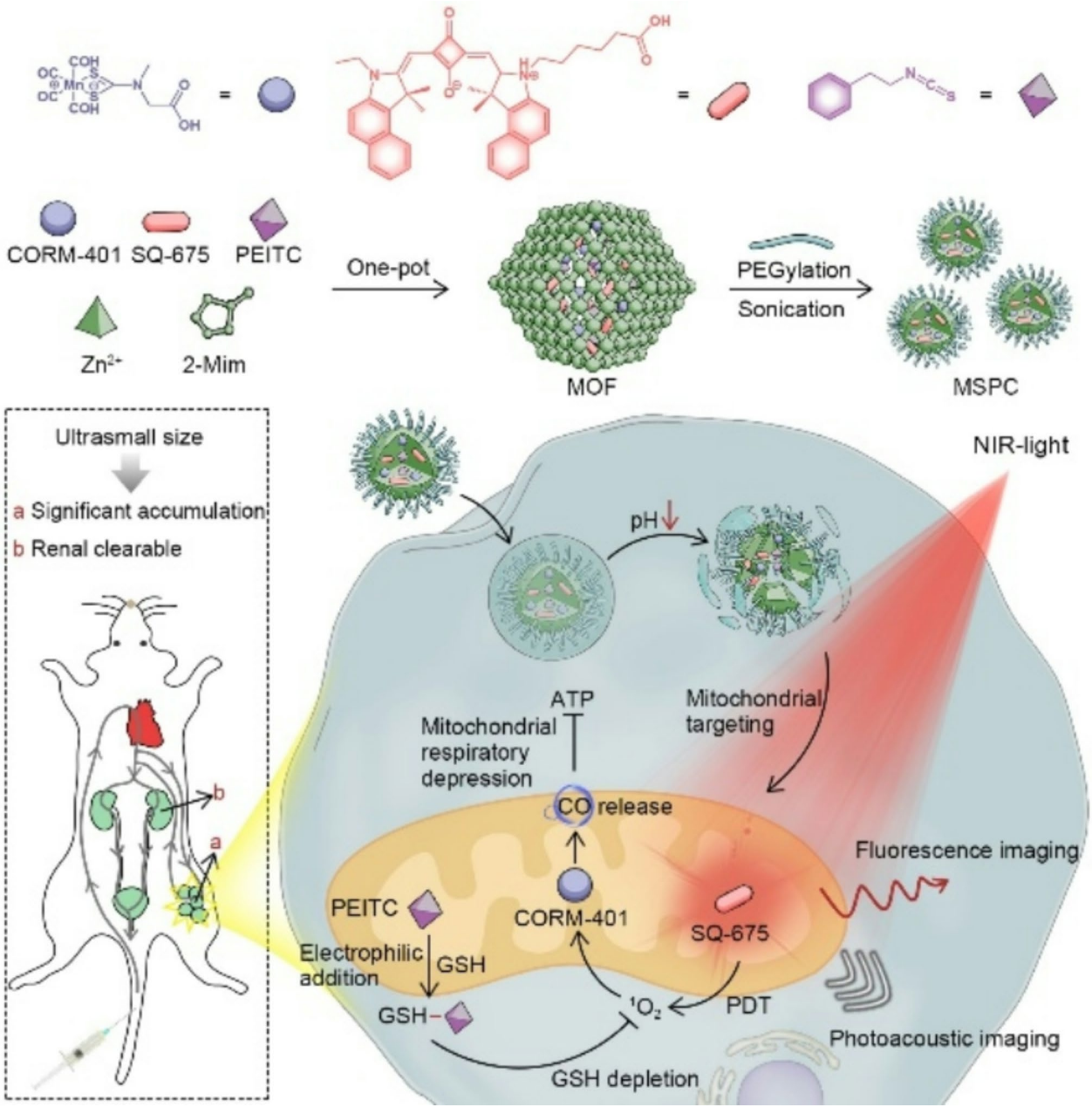

Introduction

Triple-negative breast cancer (TNBC) is a subtype of breast cancer lacking the expression of estrogen receptor, progesterone receptor, and human epidermal growth factor receptor-2 [1]. TNBC patients experience unfavorable prognoses primarily attributed to the high tumor aggressiveness and the absence of targeted therapy [2]. Metabolic reprogramming, a recently recognized characteristic of cancer, is exploited by malignant cells to fulfill the requirements of their accelerated proliferation and survival [3]. TNBC exhibits a greater reliance on aerobic glycolysis, commonly known as the Warburg effect, resulting in augmented glucose uptake and lactate secretion. This process contributes to the formation of an acidic tumor microenvironment (TME) [4]. In addition, TNBC has an increased dependence on glutamine uptake

and utilization, a condition described as "glutamine addiction" [5, 6]. The glutamine addiction indirectly supports the synthesis of abundant glutathione (GSH), which maintains intracellular redox homeostasis and protects TNBC cells from oxidative damage [7, 8]. Therefore, targeted metabolic reprogramming may become a crucial strategy in tumor treatment by interfering with GSH synthesis or depleting GSH levels, thereby enhancing the sensitivity of tumor cells and improving the effectiveness of anticancer therapies.

Photodynamic therapy (PDT) is a noninvasive therapeutic approach relying on photosensitizers to convert oxygen into reactive oxygen species (ROS) under illumination [9–13]. Recently, various porphyrins [14], squaraine dyes [15], and aggregation-induced emission photosensitizers [16–18] have been explored to enhance the treatment efficacy of PDT in TNBC. Moreover, it has been discovered that metal-organic frameworks (MOFs) could efficiently load with photosensitizers or be employed as photosensitizers for their porphyrin-like structure [19, 20]. Besides, the advantages of MOFs in drug loading and controlling release allow GSH-depleting agents to be used rationally to create photosensitizer composites [21–25]. In this study, phenethyl isothiocyanate (PEITC), a dietary substance obtained from cruciferous vegetables, was loaded into MOFs, which depletes cellular GSH by conjugating with GSH to support more efficient PDT in cancer cells [26]. Nevertheless, the damage caused by reactive oxygen species (ROS) accumulation may be transitory due to the adaptive response of TNBC metabolic reprogramming [27, 28]. Therefore, a number of studies have focused on regulating ROS toxicity with the help of ROS-triggered therapy [29–33].

Mitochondria at the core of metabolic reprogramming in TNBC are involved in various metabolic functions beyond bioenergetics [34–37]. Significantly, as the central point of cellular oxidative stress, mitochondria have crucial roles in modulating cellular redox homeostasis and closely interacting with multiple redox-sensitive pathogenesis associated with cellular demise [38]. For instance, in the presence of massive ROS, cytochrome c (Cyt C) in the sequestered intermembrane space of mitochondria, can be released into the cytosol through the influence of Bcl-2 family proteins and mitochondria permeability transition pores, which subsequently recruit and activate the caspase cascade, ultimately triggering apoptotic cell death [39]. The significant role of mitochondria in manipulating cell death through ROS has made it an attractive target for therapeutic interventions, resulting in the development of mitochondria-specific photosensitizers to enhance the efficacy of PDT [40–44]. In addition, mitochondrial metabolism inhibitors, such as CORM-401, a ROS-responsive CO donor, can disrupt the mitochondrial electron transport chain and interfere with downstream energy metabolism reactions in tumor cells [45–48]. Because CO has a high affinity for hemoglobin and is harmful to the respiratory system and healthy cells in the circulation, it is extremely desirable to transport CORM-401 to tumors and produce CO in situ in response to ROS during PDT [49–51]. However, this effective approach combining mitochondrion-targeted PDT with ROS-responsive mitochondrial metabolism-interfering therapy to enhance the lethality of ROS has not yet been described.

Herein, a multifunctional nanoprobe, named MSPC was developed by combining the GSH-depleting agent PEITC, the mitochondrion-targeted squaraine photosensitizer (SQ-675), and the ROS-responsive CO donor (CORM-401) into the acid-responsive MOF. The fabrication of our drug delivery system was through in situ encapsulation, as illustrated in Scheme 1. The MSPC preferentially accumulated in tumor tissues and could be degraded in the tumor acidic microenvironment, resulting in the release of drugs. The released PEITC can react electrophilically with thiol-containing fragments, depleting GSH in tumor cells and enhancing PDT efficacy. The released SQ-675 was expected to aggregate in the mitochondrion, achieving an aggregation-enhanced retention (AER) effect and long-term fluorescence/photoacoustic (FL/PA) imaging within the tumor. Upon exposure to near-infrared (NIR) light, SQ-675-generated ROS trigger the release of CO from CORM-401, thereby significantly reducing intracellular ATP levels by simultaneously disrupting oxidative phosphorylation and impeding aerobic glycolysis. Consequently, the combination of GSH depletion and metabolic inhibition results in an elevation of oxidative stress, ultimately enhancing the efficacy of mitochondria-targeted PDT for TNBC.

Results

Fabrication and characterization of MSPC nanodots

First, a novel NIR photosensitizer based on squaraine dye, SQ-675, was facilely synthesized, as illustrated in Figure S1-S6, Supporting Information. The SQ-675 has good solubility in organic solvents, such as methanol and dimethyl formamide (DMF), but poor solubility in aqueous solvents. The absorption and fluorescence spectra of SQ-675 measured in DMF is peaked at 675 nm and 690 nm, which clearly demonstrates the NIR dye characteristics. Furthermore, compared with the traditional photosensitizer Ce6, SQ-675 has higher photodynamic performance and photostability (Figure S7, S8, Supporting Information). To overcome water-soluble obstacles and improve the bioavailability of SQ-675, multifunctional MSPC nanodots were facilely synthesized according to the synthetic route as illustrated in Scheme 1. Compared to zeolitic imidazolate framework-8, (ZIF-8) nanocrystals with a diameter of approximately 58.0 nm,

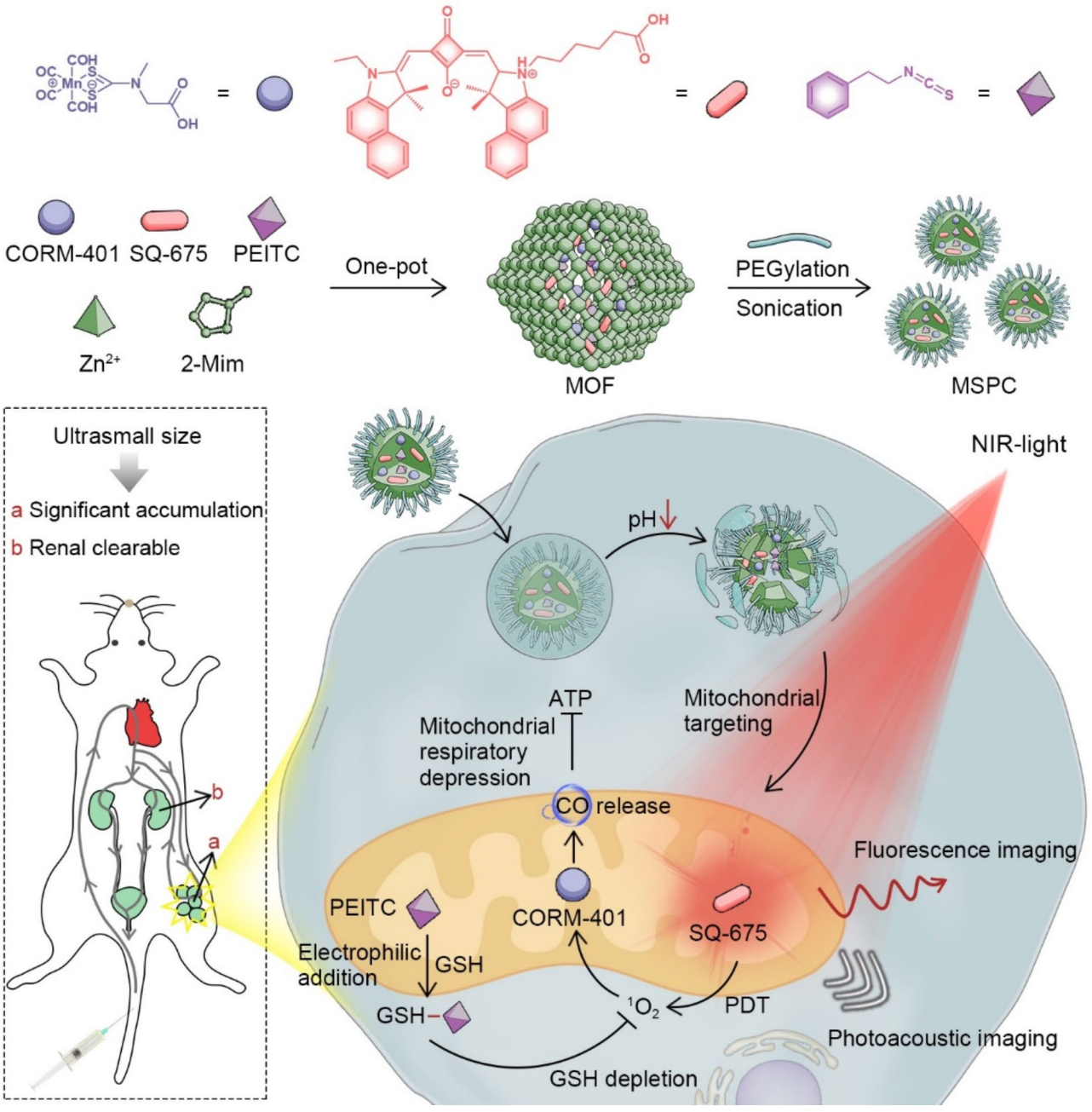

Scheme 1 Renal-clearable and tumor-retained nanodots overcoming metabolic reprogramming to boost mitochondrial-targeted PDT in TNBC

spindle-shaped nanoMOFs encapsulating the SQ-675, PEITC, and CORM-401 with an approximate diameter of 88.0 nm were prepared using a conventional method (Fig. 1A, B) [52–54]. Subsequently, an ultrasonic processor was employed to introduce liquid phase exfoliation, and the formed ultrasmall nanodots were simultaneously modified with 1,2-distearoyl-sn-glycero-3-phosphoethanolamine-N-polyethylene glycol 2000 (DSPE-PEG_{2000}) *via* the strong coordination bonds between nanodots and phosphate groups of DSPE-PEG_{2000}, which were termed MSPC nanodots [55].

The sizes of MSPC nanodots were explored by transmission electron microscope (TEM) imaging and dynamic light scattering (DLS) measurement. The TEM images demonstrated the uniform and monodispersed MSPC nanodots, measuring an average diameter of 3.0 nm, and the DLS analysis showed an average hydrodynamic size of 5.0 nm, which was below the renal filtration threshold of 5.5 nm (Fig. 1C) [56–59]. Furthermore, a notable decrease in the ζ potential values of the MSPC nanodots (-3.05 ± 0.81), in comparison to the positive ζ potential value of ZIF-8 nanocrystals (10.23 ± 0.77) and

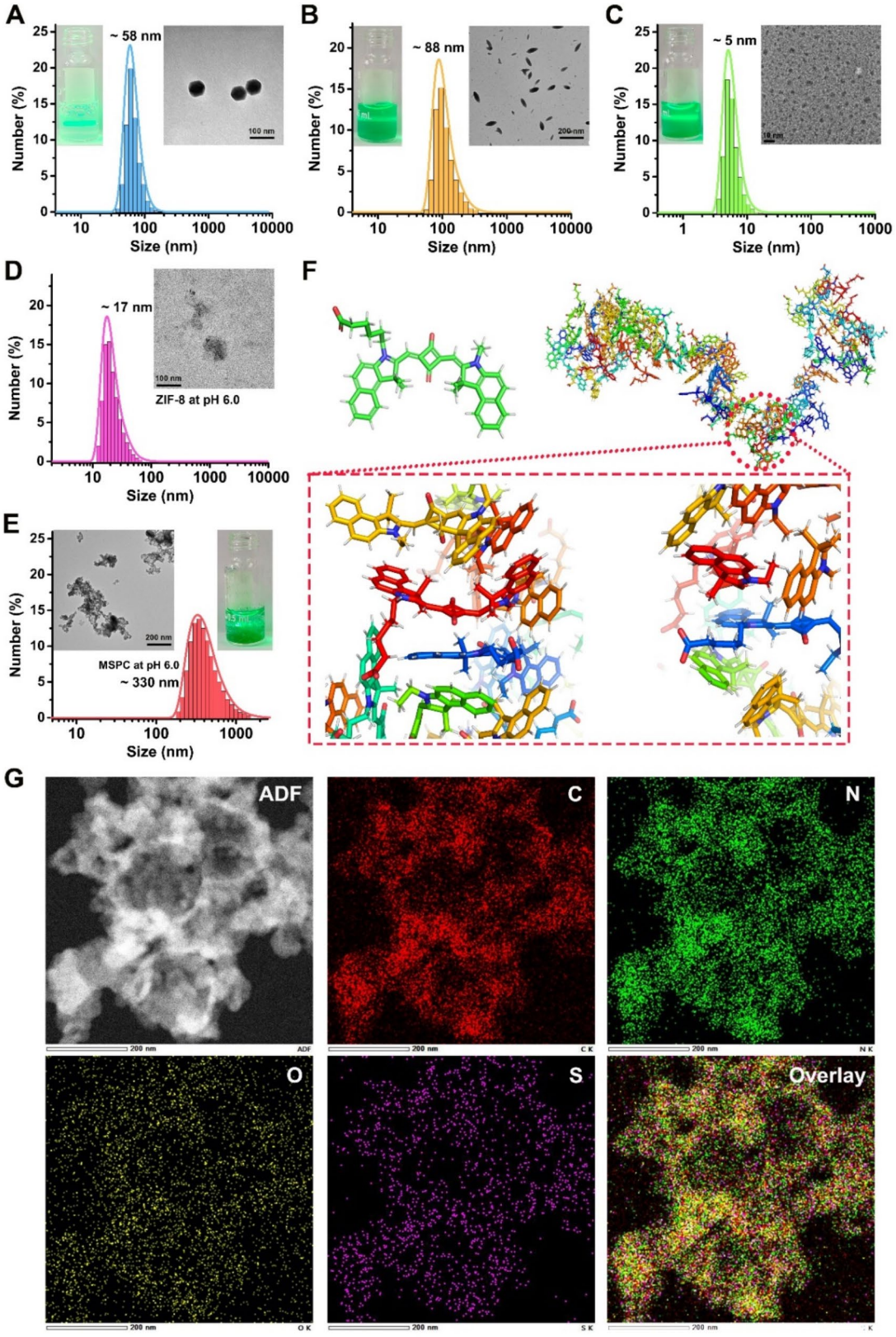

Fig. 1 (See legend on next page.)

(See figure on previous page.)

Fig. 1 Morphology and pH-response of ZIF-8 and MSPC nanodots. (**A**) Photograph, DLS and TEM of ZIF-8. (**B**) Photograph, DLS and TEM of spindle-shaped nanoMOFs. (**C**) Photograph, DLS and TEM of MSPC nanodots. (**D**) Photograph, DLS and TEM of ZIF-8 at pH 6.0. (**E**) Photograph, DLS and TEM of MSPC nanodots at pH 6.0. (**F**) The monomer structure of SQ-675 was optimized by the extended tight-binding (XTB) method, and the self-aggregated structure of SQ-675 obtained by MD simulation, as well as enlarged and rotated views of the conformation. (**G**) Elemental TEM mapping, including annular dark field (ADF), C, N, O, and S elements of MSPC at pH 6.0

the negative ζ potential value of DSPE-PEG_{2000} molecules (-9.64 ± 1.26), provided further evidence for the presence of DSPE-PEG_{2000} molecules in the MSPC nanodots (Figure S9, Supporting Information). Moreover, other formulations, including MS nanodots encapsulating the SQ-675, MSP nanodots encapsulating the SQ-675 and PEITC, and MSP nanodots encapsulating the SQ-675 and CORM-401 were synthesized using a comparable synthetic procedure, suggesting that these nanodots with an average hydrodynamic size of 5.0 nm can be easily synthesized through a facile yet efficient route, and may have higher safety with renal clearance (Figure S10, Supporting Information).

It is well-known that the ZIF-8-based nanomaterials can decompose under acidic conditions. The acidic TME-responsive collapse behaviors of ZIF-8 nanocrystals and MSPC nanodots were identified through the TEM and DLS analysis of MSPC incubated in PBS at pH 6.0. TEM and DLS results indicated that the morphology of ZIF-8 nanocrystals was destroyed under acidic conditions, with a reduced particle size of 17 nm (Fig. 1D). However, MSPC in PBS (pH 6.0) illustrates a green suspension with a substantial increase in hydrodynamic size, approximately 330 nm (Fig. 1E). Moreover, MS, MSC, and MSP nanodots in acidic PBS demonstrated a similar aggregation with hydrodynamic size around 310 nm, which may be attributed to the formation of aggregation by SQ-675 after its release from MSPC (Figure S10, Supporting Information). Furthermore, to understand the aggregation of SQ-675 in water, molecular dynamics (MD) simulation was performed with the GROMACS 2023.1 software package. Compared with the optimized geometry of a single SQ-675 molecule, the SQ-675 molecules in aqueous solvent self-assemble to form SQ-675 aggregates, in which the hydrophilic units of SQ-675 molecules are exposed in the solvent, whereas the hydrophobic aromatic groups are buried in the core (Fig. 1F) [60–62]. Meanwhile, the enlarged view and rotated view of the conformation, show SQ-675 molecules forming aggregates with intermolecular π – π stacking character. In addition, elemental TEM mapping revealed the uniformly distributed C, N, O, and S elements in the aggregation of MSPC at pH 6.0, which are all the constituent elements of SQ675, suggesting that the aggregations are formed by SQ-675 molecules released from MSPC (Fig. 1G). However, the initial assertion regarding MD modeling data is insufficient to conclusively demonstrate the formation of J-aggregates of SQ-675. The formation of J-aggregates is a complex process driven by specific molecular interactions, including hydrophobic frameworks and environmental characteristics [63].

In vitro drug release, photodynamic performance, and CO generation

The pH-responsive drug release behavior of MSPC nanodots at pH 7.4, 6.5, and 6.0 was quantitatively observed in dialysis tubes (MW cutoff of 1000 Da). As displayed in Fig. 2A, the pH value had an impact on the release rate of PEITC. Under a physiological pH of 7.4, MSPC demonstrated minimal release of PEITC (less than 10%) for up to 60 min, suggesting effective encapsulation and protection of the molecules within these MSPC, with no significant burst release. On the other hand, when the pH level was reduced to 6.0 (simulating an acidic TME), the rate of drug release increased, resulting in the release of approximately 91.34% of PEITC within 60 min. The reason behind this occurrence could be the breakdown of MSPC, resulting in an increased release of cumulative PEITC in mildly acidic environments. Consequently, the MSPC exhibits a relatively high level of stability under normal physiological conditions, while being highly sensitive to acidic TME, which prevents premature drug leakage and side effects in healthy tissues.

Furthermore, the decomposition of MSPC was identified through the analysis of absorbance and fluorescence spectra. The absorbance spectra exhibited a peak absorption at 675 nm in PBS (pH 7.4), indicating that the photophysical properties of SQ-675 were unaffected by the ultrasonic treatment and PEGylation (Fig. 2B). The emission of SQ-675 in MSPC displayed a peak at 690 nm in PBS at pH 7.4 (Fig. 2C). However, when released from MSPC under an acidic pH of 6.0, SQ-675 exhibited limited water solubility and tended to form aggregates, resulting in a significant red-shift in the absorption spectra peak from 675 nm to 680 nm and fluorescence spectral peak from 690 to 710 nm (Fig. 2D and E) [64–66]. In addition, the $^1O_2$ generation capability of MSPC was investigated using 1,3-diphenylisobenzofuran (DPBF), which undergoes decomposition in the presence of $^1O_2$, resulting in changes in its absorbance [67]. As depicted in Fig. 2F and G, the presence of MSPC at pH 6.0 and 7.4 resulted in the consumption of 75.5% and 52.6% of DPBF, respectively, following a 10-minute exposure to NIR light (1.0 mW/cm^2). These findings indicated that SQ-675 aggregates released from MSPC in acidic conditions have enhanced fluorescence and PDT performance.

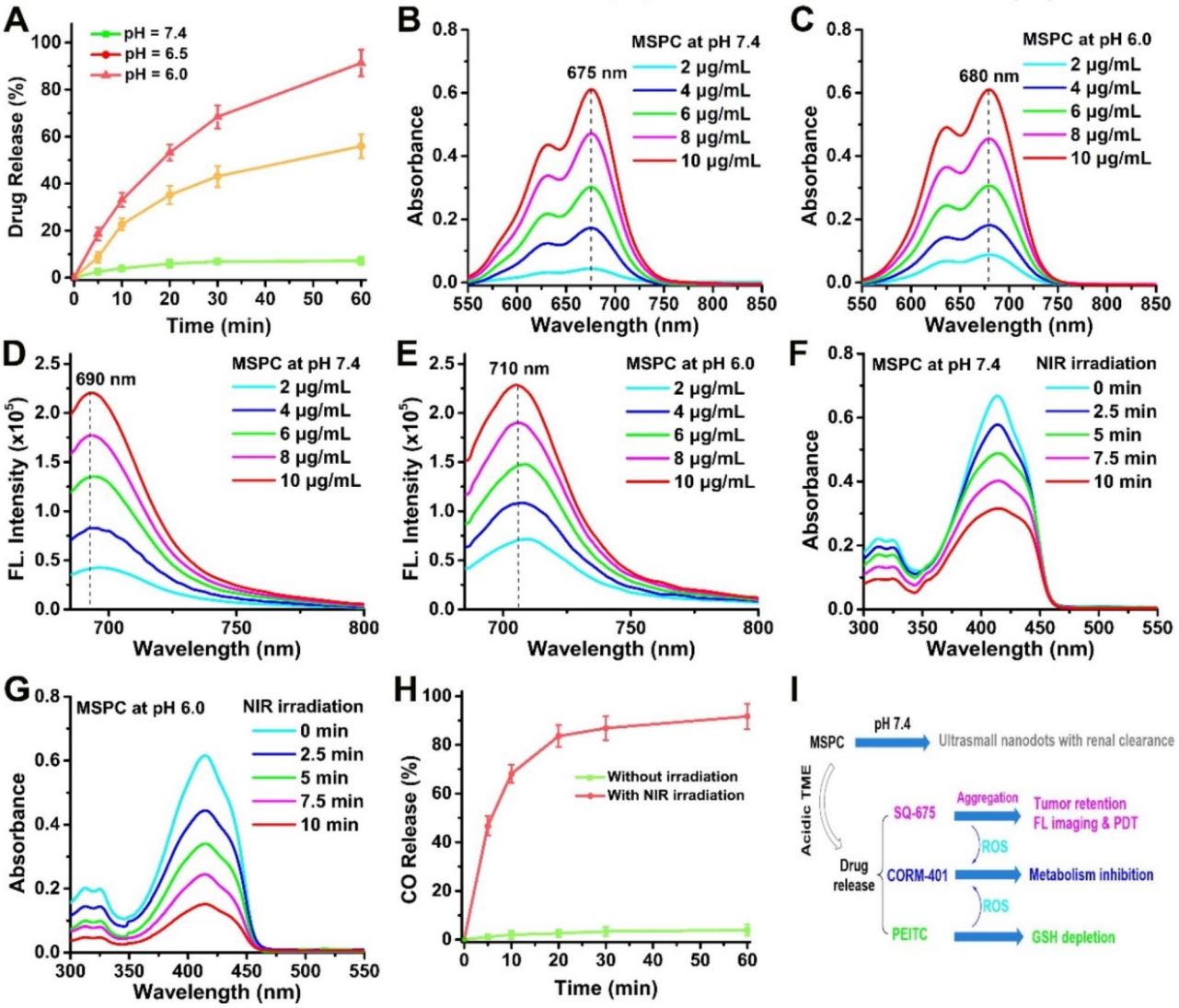

Fig. 2 Optical properties, and drug release of MSPC in the response of pH and NIR irradiation. (**A**) Acidic pH-responsive drug release profiles of MSPC. (**B, C**) Absorbance spectra and fluorescence spectra of MSPC in PBS at (**B**) pH 7.4 and (**C**) pH 6.0. (**D, E**) The fluorescence spectra of MSPC in PBS at (**D**) pH 7.4 and (**E**) pH 6.0. (**F, G**) absorbance spectra of DPBF incubated with MSPC in PBS at pH 7.4 and 6.0 after light irradiation. (**H**) The percentage of CO released from MSPC by different irradiation time. (**I**) Schematic illustration: MSPC for fluorescence imaging, pH/ROS cascade responsive chemotherapy, and PDT with prolonged tumor retention in TME. Data presents as mean ± SD, $n = 3$ (*$p < 0.05$, **$p < 0.01$, ***$p < 0.001$)

Motivated by the impressive performance of MSPC in PDT, we proceeded to investigate its potential for controlled release of CO through PDT. The release of CO from MSPC was quantified using a previously reported CO fluorescence probe, COP-1 [68]. As depicted in Fig. 2H, no CO release was observed from MSPC without laser irradiation, demonstrating that MSPC was relatively stable in PBS and could not release CO without NIR light irradiation. However, under continuous NIR light irradiation, the fluorescence intensity of COP-1 exhibited a continuous increase, indicating a sustained generation of CO gas from MSPC. These results unequivocally indicate that MSPC displays a high response to ROS generation for CO release. Thus, the SQ-675 possesses high optical contrast, making them highly advantageous for applications such as fluorescence imaging, pH/ROS cascade responsive chemotherapy, and PDT with prolonged tumor retention in TME (Fig. 2I).

Synergistic effects between mitochondria-targeted PDT and CO therapy

The cellular internalization of MSPC within 4T1 cells was examined using confocal laser scanning microscopy (CLSM), revealing a marked increase in cytoplasmic presence corresponding with extended incubation periods, thereby indicating efficient nanodot uptake *via* cellular endocytosis (Figure S11, Supporting Information). Furthermore, MSPC demonstrated a propensity

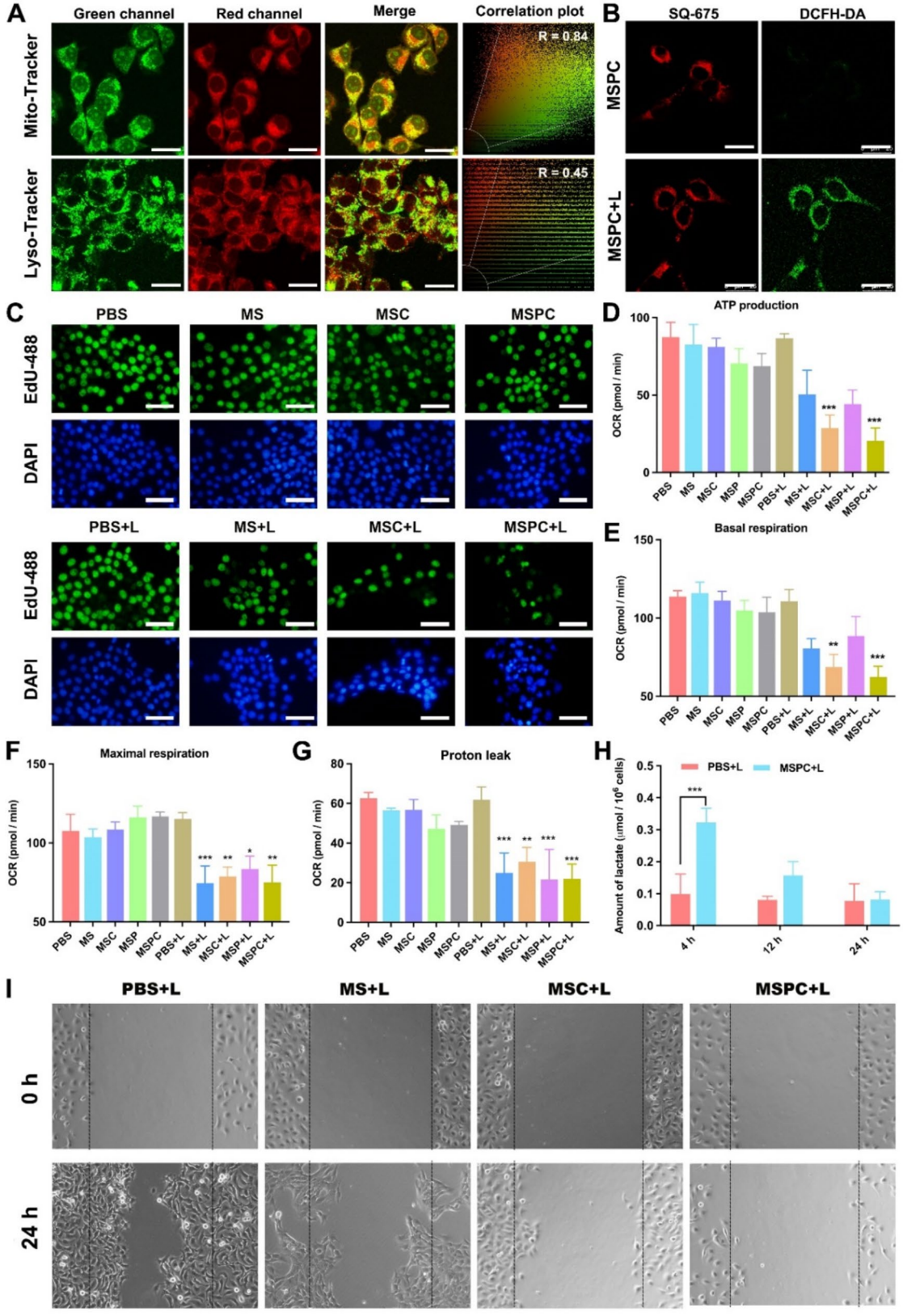

Fig. 3 (See legend on next page.)

(See figure on previous page.)

Fig. 3 Assessments of the cell uptake of MSPC and the biological effects in 4T1 cells. (**A**) CLSM pictures of 4T1 cells exposed to MSPC were co-stained with Mito-Tracker or Lyso-Tracker, along with the corresponding correlation graph depicting the relationship between the red and green fluorescence. Scale bars, 25 μm. (**B**) CLSM images of ROS levels in 4T1 cells treated with MSPC with or without light irradiation using DCFH-DA as a ROS indicator. Scale bar, 25 μm. (**C**) Cell proliferation of 4T1 cells after different treatments was detected by EdU-488 reagent. Scale bar, 100 μm. Assessment of cellular energy metabolism includes (**D**) ATP production, (**E**) basal respiration, (**F**) maximal respiration, and (**G**) proton leak. (**H**) The level of lactate in 4T1 cells treated with PBS + L or MSPC + L for different periods. Data presents as mean ± SD, $n = 3$ (*$p < 0.05$, **$p < 0.01$, ***$p < 0.001$). (**I**) The cell scratch test of 4T1 cells following treatments

for mitochondrial localization, as evidenced by Pearson's correlation coefficients (PCC) of 0.58 at 2 hours, 0.82 at 4 h, and 0.84–0.88 at 6 h (Fig. 3A and Figure S11, Supporting Information). In addition, MS, MSC, and MSP nanodots within 4T1 cells exhibited similar mitochondrial accumulation (PCC ranging from 0.86 to 0.89 at 6 h) with minimal retention in lysosomes (PCC ranging from 0.39 to 0.45 at 6 h). This suggests the potential for SQ-675 release from the nanodots, facilitating escape from acidic lysosomal environments and promoting substantial mitochondrial enrichment (Figures S12-S14, Supporting Information). Moreover, the mitochondrial targeting capabilities of SQ-675 were corroborated by observations in 4T1 cells incubated with SQ-675 for 6 h (Figure S15, Supporting Information). The intracellular ROS indicator, dichlorofluorescein diacetate (DCFH-DA), was utilized to evaluate the ROS generation by MSPC in 4T1 cells. It was observed that cells treated with MSPC exhibited bright red fluorescence of SQ-675, while displaying negligible green fluorescence of DCFH-DA, indicating minimal ROS generation (Fig. 3B). Conversely, when MSPC was combined with light irradiation (5 min, 1.0 mW/cm^2), green fluorescence was observed, providing direct evidence of ROS generation.

Moreover, the cell proliferation level was evaluated using thymidine analogue EdU-488, which detects the incorporation of EdU-488 during DNA synthesis [69]. The EdU-488 localization in the PBS group and MS group closely corresponds to DAPI, indicating a high level of cellular proliferation (Fig. 3C). The MSC and MSPC groups exhibited a slight decrease in EdU-488 levels, however, this variation did not reach statistical significance. Notably, the nuclei of the MSC + L group and MSPC group appeared concentrated and exhibited poor nuclear morphology under light illumination, with some nuclei displaying a bright blue color. The inclusion of EdU-488 was observed to be significantly hindered, providing evidence of a substantial inhibition of DNA synthesis. Furthermore, the intracellular release of CO from nanodots was assessed in 4T1 cells treated with or without NIR light irradiation, utilizing a CO indicator. The fluorescence imaging results revealed an absence of fluorescence in the PBS, MS, and MSP groups, and only weak fluorescence in the MSC and MSPC groups without NIR light irradiation. In contrast, significant intracellular fluorescence was observed in the MSC + L and MSPC + L groups following NIR light irradiation (Figure S16, Supporting Information). These findings suggest that the encapsulation of CORM-401 within the nanodots facilitates a controlled release mechanism, ensuring that CO is predominantly released in response to NIR irradiation. Furthermore, the inhibitory effects on cell proliferation in MSC + L and MSPC groups were more pronounced compared to that in MS and MSP groups, indicating a correlation between the inhibition of cell proliferation and the presence of CO.

The utilization of a cell metabolism analyzer enabled the assessment of the oxidative phosphorylation capacity of cell mitochondria through the measurement of the oxygen consumption rate (OCR) [70]. Cell metabolism analyzer can reflect the oxidative phosphorylation ability of cell mitochondria by detecting the OCR. Compared with PBS group (87.60 ± 9.44 pmol/min), MS (82.67 ± 13.06 pmol/min) or MSC (81.21 ± 5.53 pmol/min) alone had minimal impact on the ATP production level of 4T1 cells (Fig. 3D). In addition, slight decreases of ATP levels in 4T1 cells were observed in the MSP (70.47 ± 9.56 pmol/min) and MSPC (68.82 ± 8.06 pmol/min) groups. Compared with the PBS + L group (86.80 ± 2.93 pmol/min), significant inhibitions of the ATP levels were observed in the MS + L (41.71%), MSC + L (66.83%), MSP + L (49.73%), and MSPC + L (76.31%) groups. Basal respiration and maximal respiration, as depicted in Fig. 3E and F, demonstrated similarity to ATP production with obvious suppression of basal respiration in the MSC + L (39.54%), and MSPC + L (45.08%) groups. The level of proton leakage, as shown in Fig. 3G, primarily indicated the resultant damage to the mitochondria after PDT. It was observed that although ATP synthesis in the MSC + L group was lower than that in the MS + L group, there was no notable distinction in terms of mitochondrial damage. This suggests that CO could potentially induce alterations in cellular energy metabolism before the occurrence of mitochondrial structural damage. The relationship between maximal respiratory and adaptive capacity during cell stress is evident. Furthermore, the decrease in mitochondrial number under light conditions significantly inhibits the maximal respiratory capacity in all the groups.

Additionally, compared to the slight increase of the intracellular lactic acid level in 4T1 cells after MSPC + L treatment for 4 h (0.32 ± 0.044), significant decreases were subsequently observed at 12 h (0.16 ± 0.044) and 24 h (0.082 ± 0.024) (Fig. 3H). The elevated lactate

content in the MSPC + L group at 4 h can be attributed to the initial cellular response to the treatment, leading to increased glycolysis as a compensatory mechanism to maintain energy production. At 24 h, the lactate content in the MSPC + L group decreases and becomes comparable to that of the PBS + L group. This aligns with our proposed mechanism, where the combined effects of oxidative phosphorylation decoupling and inhibition of aerobic glycolysis gradually reduce lactate production over time. The initial compensatory increase in glycolysis is eventually overwhelmed by the sustained disruption of mitochondrial function and glycolytic pathways, leading to a normalization of lactate levels. Furthermore, a significant reduction in GSH levels in cells treated with MSPC and MSP nanodots, confirming that GSH depletion was successfully achieved after the PEITC uptake by cells (Figure S17, Supporting Information). Moreover, the cell scratch test (Fig. 3I) demonstrates that the invasion and metastasis abilities of the MS + L, MSC + L, and MSPC + L groups are all reduced. Notably, the MSC + L and MSPC + L groups exhibit a particularly noticeable decrease in invasion and metastasis ability. Consistent with previous research, the release of CO proves beneficial in suppressing breast cancer metastasis.

Cytotoxicity of PDT and CO gas therapy by MSPC in vitro

To examine the potential anti-tumor effects of MSPC, the viabilities of 4T1 cells at different concentrations of MS, MSC, MSP, and MSPC were assessed using the cell counting kit-8 (CCK-8) assay. Notably, without NIR light exposure, the high-concentration MS solution demonstrated no cytotoxicity towards 4T1 cells, resulting in a high cell survival rate (Fig. 4A). In contrast, the high concentration of MSC exhibited mild cytotoxicity towards 4T1 cells, with the cell survival rate surpassing 75% (Fig. 4B). The MSP with the pH-dependent release of PEITC in tumor cells showed 35.10% cell death, as well as its toxicity, is influenced by concentration. However, the cytotoxicity is not completely related to the concentration of MSPC, which may be due to GSH depletion and ROS increase in tumor cells caused by PEITC. The increased ROS is not enough to cause a stable release of CO. Under light irradiation, SQ-675 in the MS can serve as a photosensitizer, leading to 56.20% cell death at high concentrations. In comparison to MS + L, the cytotoxicity of MSP + L group was further enhanced due to the combined effect of PEITC. It is observed that MSC exhibits greater toxicity than MS under light conditions, thereby indicating that it does not hinder the PDT effect through ROS-triggered CO release. Additionally, MSC facilitates the cooperation of PDT and interferes with energy metabolism, thereby amplifying the therapeutic efficacy. Notably, compared to the other groups, MSPC + L group demonstrates the most pronounced cytotoxicity with 79.7% cell death at high concentrations, showing the synergistic therapeutic effect of PDT combined with GSH depletion and CO therapy.

To further validate the impact of MSPC on the induction of 4T1 cell death, various treatments were administered to the 4T1 cells, followed by co-staining with Calcein-AM and propidium iodide (PI) to facilitate a more intuitive observation of the distribution of viable and dead cells. As depicted in Fig. 4C, most cells in both the control group and MS group exhibited green fluorescence, indicating robust cell growth, and affirming the safety of MS. However, a slight impairment was observed in the cells treated solely with MSC, potentially attributable to the release of a limited quantity of CO triggered by endogenous ROS of tumor cells upon the administration of CORM-401 in MSC. The release of PEITC from MSP initiated by a mildly acidic pH within tumor cells, can lead to a partial reduction in cell viability. Following light illumination, MS acts as a photosensitizer and induces cell death. MSC further enhances the anti-tumor efficacy of PDT and CO under light conditions. Notably, the combination of MSPC and light treatment results in a significant cell death. The flow cytometry analysis also confirmed the synergistic effects among the components of MSPC. As shown in Fig. 4D, no significant disparity in apoptosis levels was observed between the PBS group and MS group, indicating the high safety of MS without light irradiation. However, under light irradiation, the MSPC + L group exhibited a substantial increase in the proportion of apoptotic cells, suggesting a stronger apoptosis-promoting effect compared to PDT in MS or MSP group. This enhanced effect can likely be attributed to the combined impact of PDT, GSH depletion, and CO gas therapy in combating cancer.

To comprehensively elucidate the therapeutic mechanism of MOF nanodots, particularly in their modulation of cellular metabolism and ROS levels, JC-1 staining was employed to assess alterations in mitochondrial membrane potential ($\Delta\Psi m$), a critical marker of mitochondrial integrity. The findings, illustrated in Figure S18, reveal that MOF nanodots, when subjected to NIR light irradiation, cause a marked reduction in $\Delta\Psi m$, indicative of mitochondrial dysfunction. Additionally, western blot analysis was performed to confirm the induction of pyroptosis in tumor cells. As depicted in Figure S19, there was an increase in cleaved caspase-1 and GSDMD-N levels in the MSPC + L group, corroborating the capacity of MSPC nanodots, under NIR light irradiation, to initiate ROS/caspase-1/GSDMD-dependent pyroptosis in tumor cells.

Renal-clearable and tumor-retained abilities of nanodots

To investigate the pharmacokinetics of MSPC nanodots, blood samples were collected at intervals of 5, 10, 15, 30,

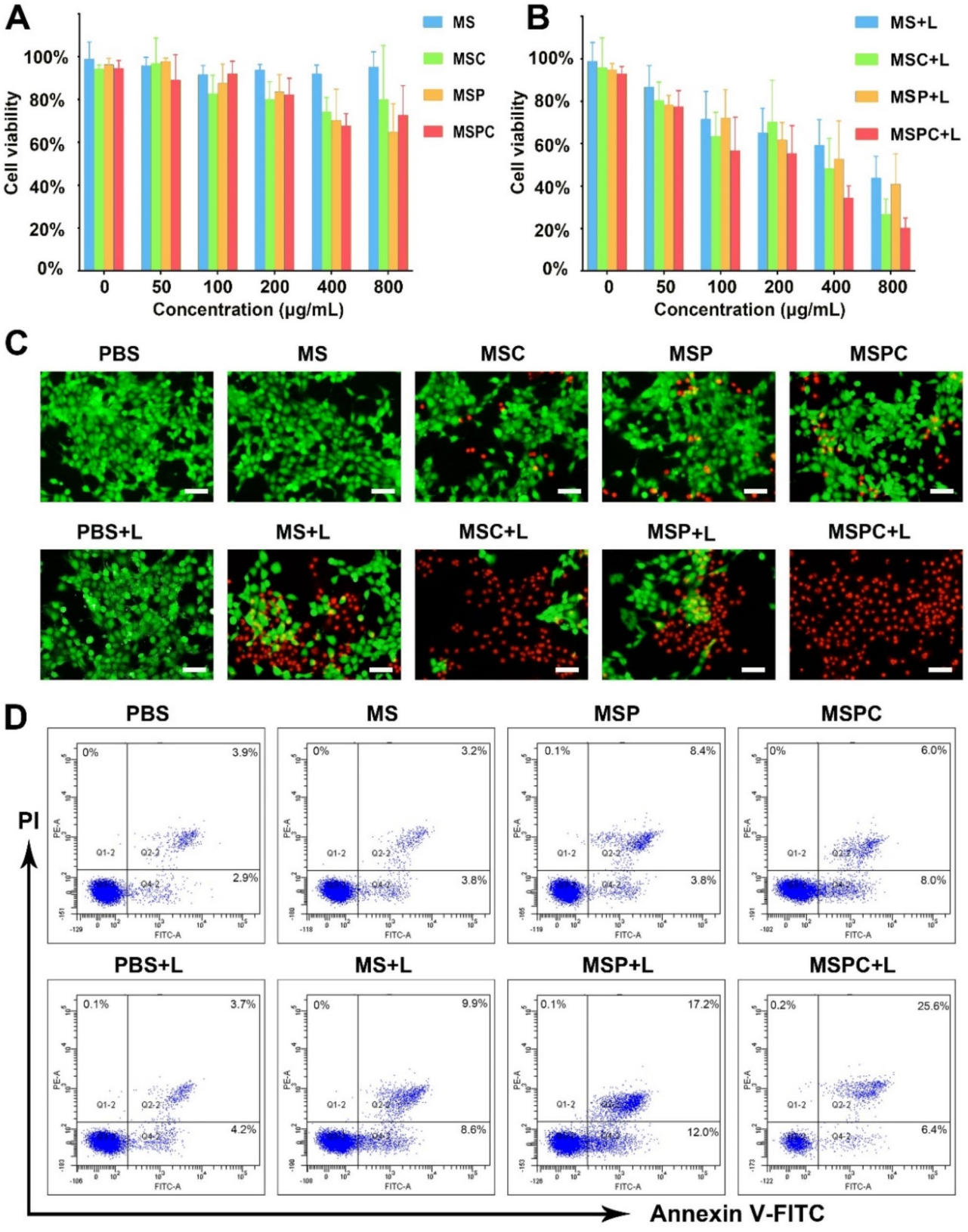

Fig. 4 Evaluations of the cytotoxicity of the combined PDT and CO gas therapy. (**A**) Cell viabilities of 4T1 cells treated with MS, MSC, MSP or MSPC. (**B**) Cell viabilities of 4T1 cells treated with MS, MSC, MSP or MSPC plus light irradiation (5 min, 1.0 mW/cm^2). (**C**) Fluorescence imaging based on calcein-AM (green fluorescence, living cells) /PI (red fluorescence, dead cells) double staining of 4T1 cells after treatments. Scale bar, 100 μm. (**D**) Apoptosis analyses of 4T1 cells after different treatments were performed using flow cytometry

45, 60, 90, and 120 min following the injection of MSPC nanodots. The zinc content in the collected blood samples was quantified using inductively coupled plasma-mass spectrometry (ICP-MS) after microwave digestion of the samples. As illustrated in Figure S20A, the blood concentration curves indicated a rapid decline in MSPC nanodot concentrations over a 120-minute period, suggesting rapid systemic clearance and elimination from the body. To evaluate renal clearance, urine and feces were collected from the mice over a 24-hour period and analyzed *via* ICP-MS. As depicted in Figure S20B, zinc ions from MSPC excreted in urine constituted 63.7 ± 4.1% of the injected dose per gram (ID/g) at 24 h post-injection in mice. At 24 h post-injection, the mice were euthanized, and the residual zinc in major organs was quantified by ICP-MS following microwave digestion of the tissues. The residual zinc ions predominantly accumulated in the kidneys and liver, with negligible levels detected in other organs.

Fluorescence imaging was conducted in mice harboring 4T1 tumors. As depicted in Fig. 5A, the fluorescence signal in the tumor region exhibited an increase at 2 h after injection, indicating the selective accumulation of nanodots in the tumor area. In all groups, the fluorescence intensity in the tumor reached its maximum at 12 h post-injection and remained robust over 9 days (Fig. 5B). These findings demonstrate that nanodots, especially MSPC, exhibit superior aggregation and fluorescence enhancement effects in acidic tumor environments. Consequently, MSPC enables prolonged retention and high-contrast imaging of tumor tissue. Figure 5C illustrates the three-dimensional (3D) fluorescence imaging reconstruction at 9 days post-injection of MSPC. Notably, the tumor exhibits strong fluorescence intensity, while only minimal fluorescence signals are observed in the kidneys. Importantly, no discernible fluorescence signals are detected in other normal tissues, indicating minimal non-specific uptake of MSPC.

Considering the ultrasmall size and remarkable responsiveness to the acidic microenvironment of tumors, it is anticipated that MSPC will accumulate in tumor sites and undergo renal metabolism to mitigate prolonged retention and toxicity. The bio-distribution of MSPC in the major organs and tumors was measured by ex vivo FL imaging. As anticipated, a significantly intense fluorescence signal persisted in the tumor region at 9 d post-injection of MSPC (Fig. 5D). Notably, only a negligible quantity of MSPC was observed in the kidney, suggesting that MSPC can be eliminated *via* the renal pathway owing to its extremely small size (Fig. 5E). These findings demonstrate the effective accumulation of MSPC at the tumor site and its subsequent elimination through the kidney.

Photoacoustic (PA) imaging is a novel type of non-invasive biomedical imaging technology that offers enhanced tissue penetration and spatial resolution compared to fluorescence imaging. To ascertain the accumulation and penetration of MSPC in tumors, in vivo PA imaging was conducted, taking advantage of the NIR absorption of MSPC (Fig. 5F). PA images of mice were obtained at different time intervals, and the corresponding PA intensities at the tumor location were quantified using a PA instrument. As depicted in Fig. 5G, the signal intensities of PA imaging gradually increased over time and reached their peaks at 12 h post-injection, indicating the successful accumulation of MS and MSPC in the tumor. This observation aligns with the results obtained from FL imaging. More importantly, it was discovered that the PA signal intensities of MSPC within the tumor region were significantly greater than those of the MS group, which may be attributed to the release of CO induced by ROS from MSPC. These findings provide compelling evidence for the substantial accumulation of MSPC at tumor sites and highlight their promising potential for cancer treatment.

To assess the biosafety, a hemolysis test was performed to examine the potential for red blood cell damage (Figure S21, Supporting Information). Additionally, we have evaluated liver and kidney function indicators, including alkaline phosphatase (ALP), alanine aminotransferase (ALT), aspartate aminotransferase (AST), creatinine (CREA), urea, and creatine kinase (CK) levels, in the treated animals (Figure S22, Supporting Information). The results demonstrate that the MSPC nanodots exhibit excellent biocompatibility with no significant adverse effects on liver and kidney function or hemolytic activity.

Anti-tumor efficacy of self-cascaded chem-PDT and CO gas therapy

The increased retention of photosensitizers within tumors, facilitated by AER, extends the effective time window for image-guided PDT. FL/PA imaging guides the treatments of tumor-bearing mice, allowing for an extended and optimized time frame to administer three PDT sessions following a single-dose injection of MOF nanodots To assess the in vivo therapeutic effectiveness of the combined treatments, 4T1-Luc tumor-bearing mice in 10 groups ($n = 4$) were injected with PBS, MS, MSC, MSP, and MSPC (100 μL, 1 mg/mL) *via* the tail vein, respectively. Afterwards, mice in PBS + L, MS + L, MSP + L, MSC + L, MSPC + L groups were irradiated with NIR laser (5 min, 2.0 mW/cm^2). As illustrated in Fig. 6A, after injection of one dose of PBS or MOF nanodots at Day 0, the mice received three sessions of PDT at the next three days. This approach may significantly mitigate systemic toxicity associated with repeated administrations and enhance the therapeutic efficacy of combination

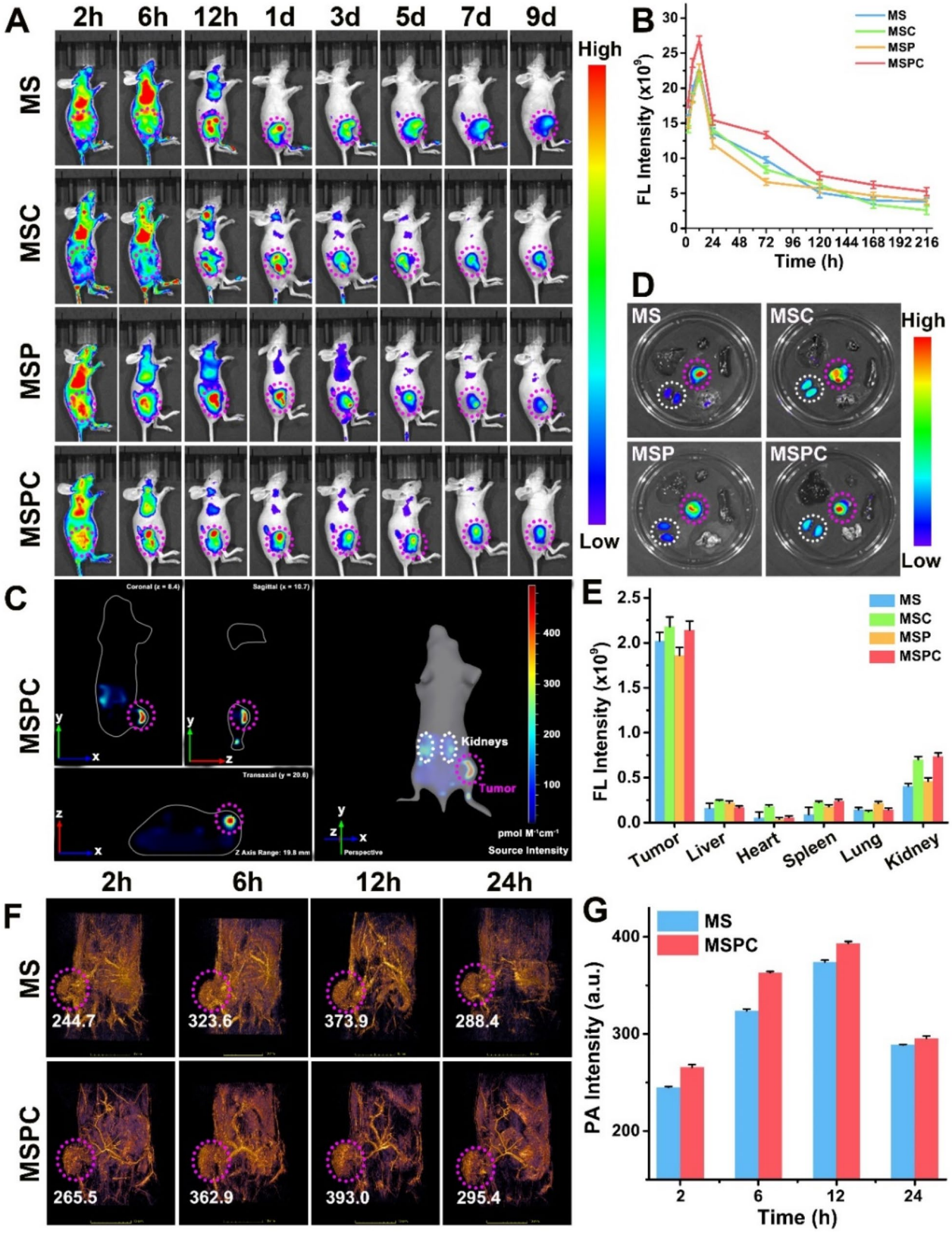

Fig. 5 FL/PA images of 4T1 tumor model in vivo and ex vivo. (**A**) In vivo FL imaging of 4T1 tumor-bearing mice was performed in vivo at 2 h, 6 h, 12 h, 1 day (**d**), 3 d, 5 d, 7 d, and 9 d after intravenous injection of MS, MSP, MSC, or MSPC. (**B**) Fluorescence intensities in the tumor areas of mice. (**C**) 3D virtual refocusing of FL imaging at 9 d post-injection. (**D**) Ex vivo FL imaging and (**E**) FL intensities of organs and tumors from mice at 9 d post-injection. (**F**) PA imaging and (**G**) the PA signal intensity in tumor areas of mice treated with MS or MSPC, respectively

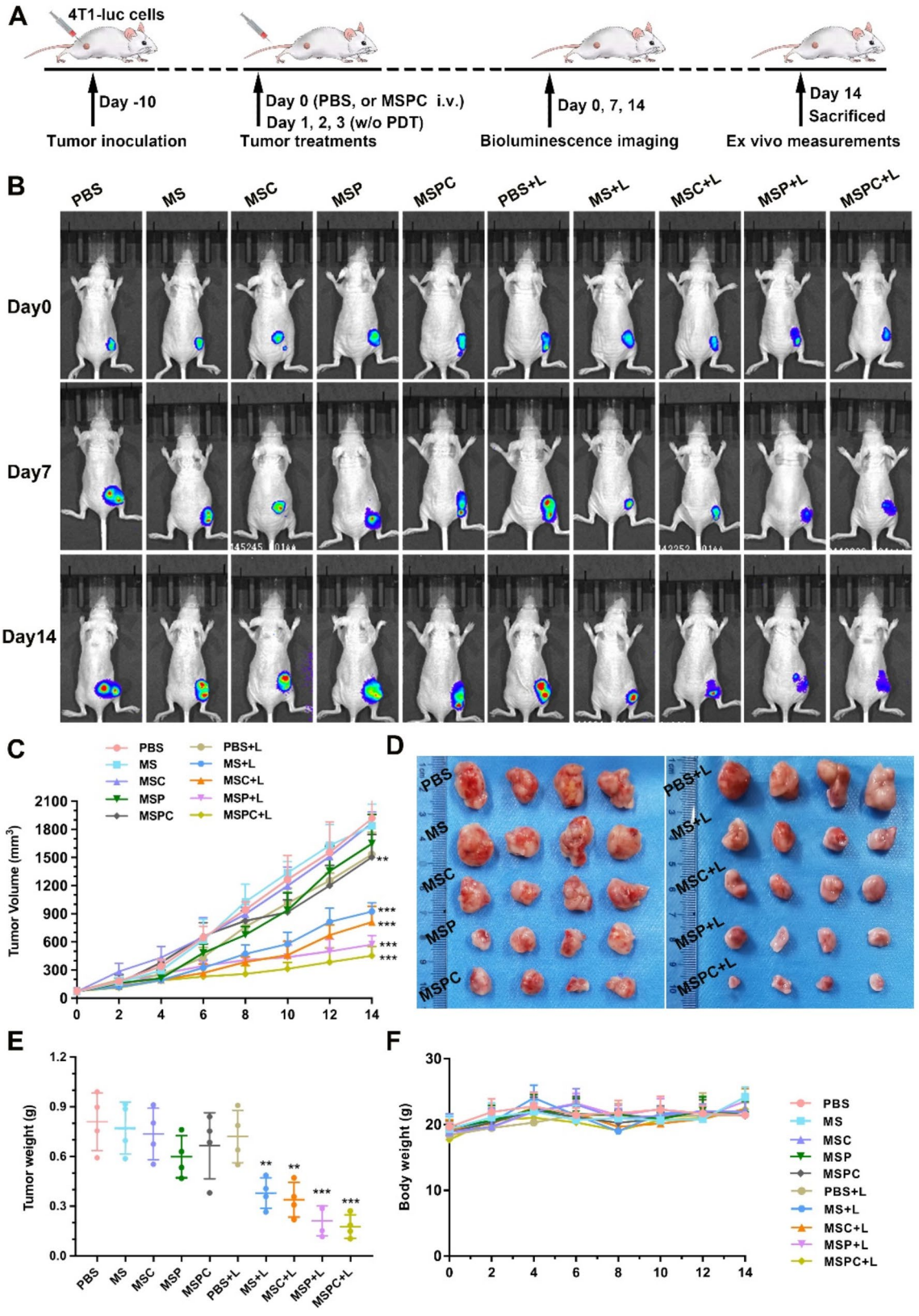

Fig. 6 In vivo anti-cancer properties of MSPC. (**A**) Illustration showing the inoculation of 4T1-Luc tumors, combined therapies, and BL imaging in BALB/c mice. (**B**) In vivo BL imaging of mice in the various groups. (**C**) The tumor volume, (**D**) The image of tumors, (**E**) the weights of tumors, and (**F**) the body weights of mice. Data presents as mean ± SD, $n = 4$ (*$p < 0.05$, **$p < 0.01$, ***$p < 0.001$)

treatments. Meanwhile, weekly bioluminescence (BL) imaging was performed to monitor tumor proliferation. The recorded BL images demonstrated the rapid proliferation of tumors in the PBS group (Fig. 6B). Additionally, a continuous increase in BL signal at the tumor region was observed in both the PBS + L group and the groups without light irradiation, indicating that tumor growth was not inhibited. However, the MS + L, MSP + L, and MSC + L groups exhibited a gradual decrease in BL signals, with the MSC + L group displaying the lowest BL signal at the end of the study, suggesting that MSPC + L has superior anti-tumor efficacy compared to the other groups. As depicted in Fig. 6C, compared to the PBS control, no tumor suppression was observed in MS and MSC groups. On one hand, the mice in the MSP and MSPC groups demonstrated a marginal reduction in tumor growth by 16.57% and 18.32%, suggesting that GSH depletion by PEITC alone had a restricted therapeutic impact. On the other hand, the MSC + L (55.91%) groups showed more remarkable tumor suppression than the MS + L group (49.67%), potentially due to ROS production leading to CO release. More importantly, the MSP + L group (68.84%) exhibited a significant tumor growth delay, and the disparity between MSPC and the other groups became increasingly apparent over time. Finally, MSPC + L achieved the most impressive result in inhibiting 75.44% of tumors, demonstrating the dominant effectiveness of self-cascaded chemo-PDT and CO gas treatment.

At the end of therapy, the exfoliated tumors provided a more intuitive depiction of the treatment effects in each group, with MSPC + L treatment demonstrating the most significant efficacy (Fig. 6D). Additionally, the average weight of exfoliated tumors in the MSPC + L group was merely 24.48% of the control group treated with PBS + L and 45.56% of the MS + L group, indicating a higher tumor inhibition rate (TIR) of 75.52% in the MSPC + L group (Fig. 6E). Furthermore, the H&E analysis demonstrated significant cell shrinkage and nucleus condensation following MSPC + L therapy, and Ki67 immunohistochemical staining further confirmed the efficient destruction of tumors in the MSPC + L group (Fig. 7). Additionally, the decrease in Ki67 and increase in TUNEL staining assays provided further evidence of effective tumor destruction in the MSPC + L group (Fig. 7 and Figure S23, Supporting Information). Besides, mice weight and H&E analysis of organs among all treatment groups indicated no significant variances, affirming the lack of observable adverse reactions throughout the treatment (Figs. 6F and 7). These findings support the notion that the combined chemo-PDT and CO gas therapy exhibit synergistic effects against TNBC.

Discussion

In contrast to normal cells, tumor cells necessitate the reprogramming of their metabolic phenotype to acquire additional nourishment and energy for sustaining their accelerated cell proliferation. Consequently, the manipulation of tumor cell energy metabolism through antitumor therapy has garnered significant attention from researchers over the past decade. Particularly noteworthy is the "starvation therapy," wherein glucose oxidase is employed to deplete exogenous glucose, thereby depriving tumor cells of their primary energy source. However, recent research has revealed that tumor metabolism exhibits heterogeneity and adaptability, rendering the mere inhibition of glycolysis therapy insufficient in completely impeding ATP supply. Tumor cell proliferation, invasion, and metastasis are still sustained by ATP derived from alternative sources such as energy metabolism from lactic acid, glutamine, and pyruvate. Furthermore, in comparison to receptor-positive breast cancer subtypes, TNBC exhibits greater reliance on aerobic glycolysis, fatty acid synthesis, and glutaminolysis for proliferation, while displaying reduced sensitivity to enzyme inhibitors that target glucose transport.

CO gas could competitively bind to the oxygen binding site and cytochrome c oxidase, thereby impeding the subsequent cellular energy metabolism reaction, obstructing the mitochondrial electron transfer chain, and inhibiting mitochondrial respiratory function, ultimately leading to a significant reduction in cellular ATP production. The interference of CO in cellular energy metabolism can potentially enhance the effectiveness of chemotherapy and PDT, offering a distinctive approach in the treatment of TNBC. Nevertheless, despite the existing research on the utilization of CO for anti-tumor and metastasis inhibition, the clinical utility of CO is constrained by certain inherent drawbacks. CO exhibits a high yet untargeted transmembrane diffusion ability, thereby posing a risk of CO poisoning in normal tissues when blood concentration is elevated. Additionally, the gaseous nature of CO makes it challenging to accumulate at the tumor site, resulting in limited therapeutic efficacy and even promoting tumor metastasis.

To address these limitations, the MOF platform was employed to modify the chemotherapy drug PEITC, photosensitizer SQ-675, and CO-releasing molecule CORM-401. Under specific light irradiation, PDT can generate ROS that stimulate MSPC to release CO. This investigation has confirmed that PDT and the subsequent release of CO can cause irreversible damage to the mitochondria of tumor cells, leading to cell death. In comparison to previous studies, the MSPC-based anti-tumor strategy offers several advantages. Firstly, MSPC possesses an appropriate particle size and can be metabolized by the kidney. Additionally, drugs released from MSPC in

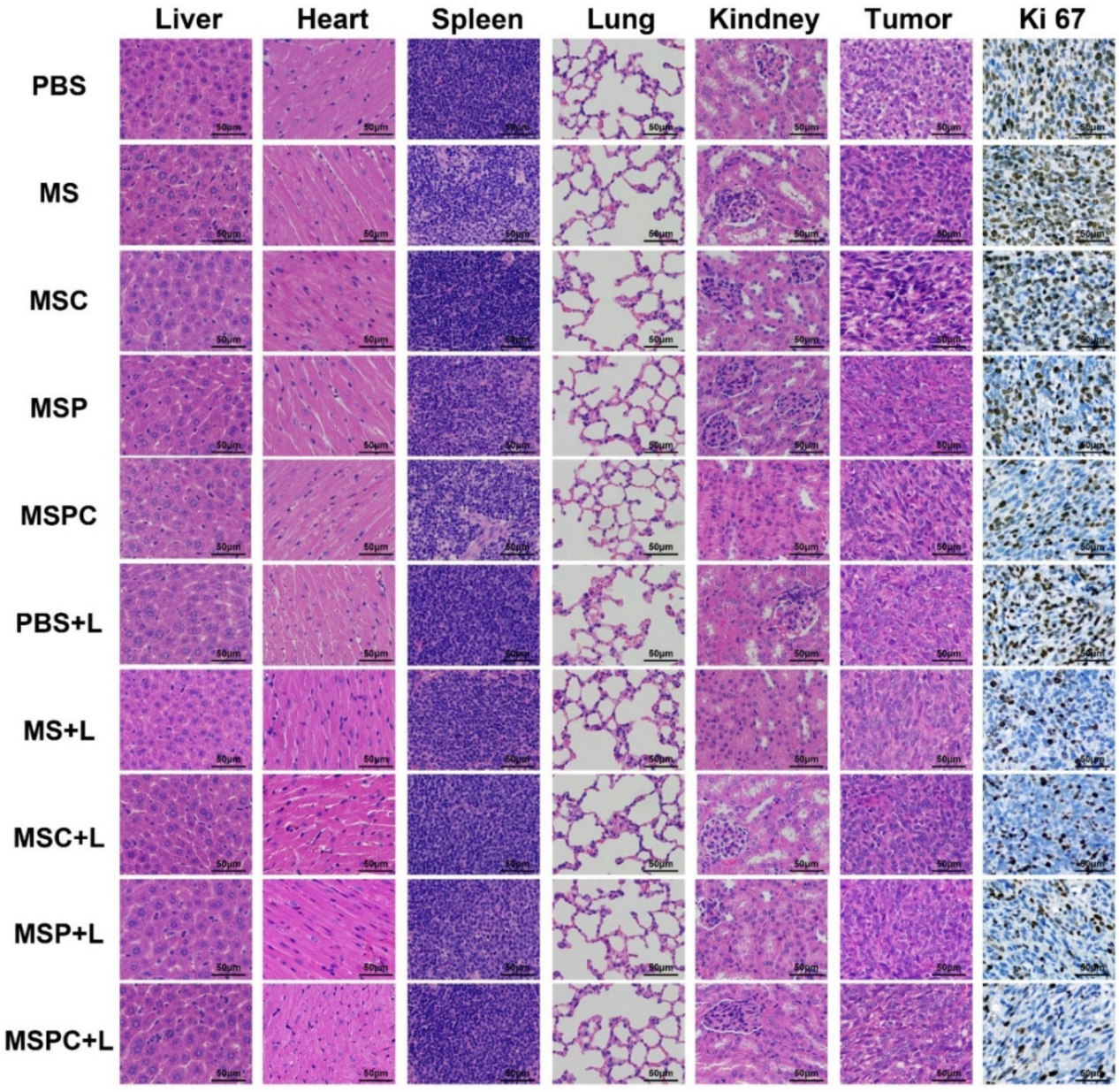

Fig. 7 Representative H&E of organs and tumor slides, as well as Ki67 immunohistochemical staining of tumor slides. Scale bar is 50 μm

the acidic tumor region, enable rapid in vivo clearance while maintaining retention within the tumor. The specific accumulation of therapeutic agents in tumor areas can address the limitation of diffusion distance and mitigate the adverse effects of CO and ROS. This approach can enhance the therapeutic efficacy of PDT and CO gas by inducing metabolic pathway alterations in TNBC cells. Furthermore, the intracellular release of CO triggered by PDT does not compromise the anti-tumor effect of PDT. Additionally, the enhanced retention of photosensitizers within tumors, enabled by the AER effect, prolongs the timeframe for long-term FL/PA imaging-guided PDT in the treatment of TNBC. The PDT, sensitized by MSPC, results in a substantial delay in tumor growth following a single-dose administration and allows for repeatable PDT. Consequently, the combined application of PDT and CO can synergistically exploit energy deficiency caused by CO and mitochondrial damage induced by PDT, thereby maximizing the therapeutic outcome.

Conclusion

In conclusion, the utilization of MSPC demonstrates notable attributes such as prolonged retention and infiltration within tumors, swift renal clearance in vivo,

commendable biological safety, and effective anti-tumor capabilities. Under acidic conditions, MSPC exhibits the ability to degrade or undergo structural breakdown, thereby facilitating drug release. Additionally, the inclusion of PEITC aids in the depletion of GSH within tumor cells, consequently enhancing the efficacy of PDT generated by SQ-675. The resulting ROS generated by PDT further triggers the release of CO from CORM-401, thereby disrupting energy metabolism, inhibiting ATP production within tumor cells, and ultimately inducing cell death through a collaborative mechanism. This presents a novel avenue for the exploration of diagnosis and treatment options for TNBC.

Supplementary Information

The online version contains supplementary material available at https://doi.org/10.1186/s12951-025-03264-7.

Supplementary Material 1

Author contributions

D. Y., Y. W.: Investigation, Writing-original draft. X. D., Y. H., W. H. and Y. C.: Validation, Visualization. D.-K. J. and R. Z.: Methodology. D. W.: Supervision, Writing-review & editing. All authors read and approved the final manuscript.

Funding

This work was supported by the National Natural Science Foundation of China (92159203, 82471976, 82472039, 82071870), the Sponsored Program of Shanghai Science and Technology Committee (No. 24TS1415300), and the Shanghai Rising-Star Program (22QA1406000).

Data availability

No datasets were generated or analysed during the current study.

Declarations

Ethical approval

The ethical review board of the XinHua Hospital Affiliated to Shanghai JiaoTong University School of Medicine, China, approved the experiment protocol and strictly followed its guidelines (Ethical approval number: XHEC-F-2023-014).

Consent to participate and publication of human face

The authors affirm that human research participant has provided informed consent for publication of human face. Signed participant publication approval was obtained from the participate.

Consent for publication

All authors read and agreed to submit the manuscript.

Competing interests

The authors declare no competing interests.

Author details

[1]Department of Radiology, Xinhua Hospital, Shanghai Jiao Tong University School of Medicine, Shanghai 200092, China
[2]College of Health Science and Technology, Shanghai Jiao Tong University School of Medicine, Shanghai 200025, China
[3]Institute of Molecular Medicine (IMM), Renji Hospital, Shanghai Jiao Tong University School of Medicine, Shanghai 200240, China
[4]Department of Physics and Astronomy, Uppsala University, Box 516, Uppsala SE-751 20, Sweden

Received: 3 December 2024 / Accepted: 20 February 2025
Published online: 10 March 2025

References

1. Al-Mahmood S, Sapiezynski J, Garbuzenko OB, Minko T. Metastatic and triple-negative breast cancer: challenges and treatment options. Drug Deliv Transl Res. 2018;8:1483–507.
2. Yin L, Duan J-J, Bian X-W, Yu S. Triple-negative breast cancer molecular subtyping and treatment progress. Breast Cancer Res. 2020;22:61–73.
3. Faubert B, Solmonson A, DeBerardinis RJ. Metabolic reprogramming and cancer progression. Science. 2020;368:eaaw5473.
4. Wang Z, Jiang Q, Dong C. Metabolic reprogramming in triple-negative breast cancer. Cancer Biol Med. 2020;17:44–59.
5. Li S, Zeng H, Fan J, Wang F, Xu C, Li Y, et al. Glutamine metabolism in breast cancer and possible therapeutic targets. Biochem Pharmacol. 2023;210:115464.
6. Wu M, Wang Q, Chen S, Zhou Z, Li J, Sun H, et al. Metabolic intervention liposome for targeting glutamine-addiction of breast cancer. J Controlled Release. 2022;350:1–10.
7. Delgir S, Bastami M, Ilkhani K, Safi A, Seif F, Alivand MR. The pathways related to glutamine metabolism, glutamine inhibitors and their implication for improving the efficiency of chemotherapy in triple-negative breast cancer. Mutat Res Mutat Res. 2021;787:108366.
8. Quek L-E, van Geldermalsen M, Guan YF, Wahi K, Mayoh C, Balaban S, et al. Glutamine addiction promotes glucose oxidation in triple-negative breast cancer. Oncogene. 2022;41:4066–78.
9. Pham TC, Nguyen V-N, Choi Y, Lee S, Yoon J. Recent strategies to develop innovative photosensitizers for enhanced photodynamic therapy. Chem Rev. 2021;121:13454–619.
10. Xie J, Wang Y, Choi W, Jangili P, Ge Y, Xu Y, et al. Overcoming barriers in photodynamic therapy Harnessing nano-formulation strategies. Chem Soc Rev. 2021;50:9152–201.
11. Chen J, Fan T, Xie Z, Zeng Q, Xue P, Zheng T, et al. Advances in nanomaterials for photodynamic therapy applications: status and challenges. Biomaterials. 2020;237:119827.
12. Tang Y, Bisoyi HK, Chen X, Liu Z, Chen X, Zhang S, et al. Pyroptosis-Mediated synergistic photodynamic and photothermal immunotherapy enabled by a Tumor-Membrane-Targeted photosensitive dimer. Adv Mater. 2023;35:202300232.
13. Tang Y, Wang Z, Li Q. Pyroptosis of breast Cancer stem cells and immune activation enabled by a multifunctional prodrug photosensitizer. Adv Funct Mater. 2024;34:202405367.
14. Tian J, Huang B, Nawaz MH, Zhang W. Recent advances of multi-dimensional porphyrin-based functional materials in photodynamic therapy. Coord Chem Rev. 2020;420:213410.
15. Ilina K, MacCuaig WM, Laramie M, Jeouty JN, McNally LR, Henary M. Squaraine dyes: molecular design for different applications and remaining challenges. Bioconjug Chem. 2020;31:194–213.
16. Cen P, Huang J, Jin C, Wang J, Wei Y, Zhang H, et al. Aggregation-induced emission luminogens for in vivo molecular imaging and theranostics in cancer. Aggregate-. 2023;4:e352.
17. Tang Y, Wang X, Zhu G, Liu Z, Chen X, Bisoyi HK, et al. Hypoxia-Responsive photosensitizer targeting dual organelles for photodynamic therapy of tumors. Small. 2023;19:202205440.
18. Tang Y, Wang X, Chen S, Li Q. Photoactivated theranostic nanomaterials based on aggregation-induced emission luminogens for cancer photoimmunotherapy. Responsive Mater. 2024;2:20240003.
19. Zhang X, Wasson MC, Shayan M, Berdichevsky EK, Ricardo-Noordberg J, Singh Z, et al. A historical perspective on porphyrin-based metal-organic frameworks and their applications. Coord Chem Rev. 2021;429:213615.
20. Chen J, Zhu Y, Kaskel S. Porphyrin-Based Metal-Organic frameworks for biomedical applications. Angew Chem Int Ed. 2021;60:5010–35.
21. He S, Wu L, Li X, Sun H, Xiong T, Liu J, et al. Metal-organic frameworks for advanced drug delivery. Acta Pharm Sin B. 2021;11:2362–95.
22. Wang Y, Yan J, Wen N, Xiong H, Cai S, He Q, et al. Metal-organic frameworks for stimuli-responsive drug delivery. Biomaterials. 2020;230:119619.
23. Wang Y, Wu W, Mao D, Teh C, Wang B, Liu B. Metal-Organic framework assisted and tumor microenvironment modulated synergistic Image-Guided Photo-Chemo therapy. Adv Funct Mater. 2020;30:2002431.

24. Wang L, Xu Y, Liu C, Si W, Wang W, Zhang Y, et al. Copper-doped MOF-based nanocomposite for GSH depleted chemo/photothermal/chemodynamic combination therapy. Chem Eng J. 2022;438:135567.
25. Niu B, Liao K, Zhou Y, Wen T, Quan G, Pan X, et al. Application of glutathione depletion in cancer therapy: enhanced ROS-based therapy, ferroptosis, and chemotherapy. Biomaterials. 2021;277:121110.
26. Gupta P, Wright SE, Kim S-H, Srivastava SK. Phenethyl isothiocyanate: A comprehensive review of anti-cancer mechanisms. Biochim Biophys Acta BBA - Rev Cancer. 2014;1846:405–24.
27. Nakamura H, Takada K. Reactive oxygen species in cancer: current findings and future directions. Cancer Sci. 2021;112:3945–52.
28. Saikolappan S, Kumar B, Shishodia G, Koul S, Koul HK. Reactive oxygen species and cancer: A complex interaction. Cancer Lett. 2019;452:132–43.
29. Huang Z, Ding Y, Luo Y, Chen M, Zeng Z, Zhang T, et al. ROS-triggered cycle amplification effect: A prodrug activation nanoamplifier for tumor-specific therapy. Acta Biomater. 2022;152:367–79.
30. Wang S, Yu G, Yang W, Wang Z, Jacobson O, Tian R, et al. Photodynamic-Chemodynamic cascade reactions for efficient drug delivery and enhanced combination therapy. Adv Sci. 2021;8:2002927.
31. Su X, Zhuang W, Yu T, He H, Ma B, Chen L, et al. ROS and GSH Dual-Responsive GEM prodrug micelles for ROS-Triggered fluorescence turn on bioimaging and Cancer therapy. Adv Mater Interfaces. 2020;7:2000294.
32. Uthaman S, Pillarisetti S, Mathew AP, Kim Y, Bae WK, Huh KM, et al. Long Circulating photoactivable nanomicelles with tumor localized activation and ROS triggered self-accelerating drug release for enhanced locoregional chemo-photodynamic therapy. Biomaterials. 2020;232:119702.
33. Wu P, Dong W, Guo X, Qiao X, Guo S, Zhang L, et al. ROS-Responsive blended nanoparticles: Cascade-Amplifying synergistic effects of sonochemotherapy with On-demand boosted drug release during SDT process. Adv Healthc Mater. 2019;8:1900720.
34. Weiner-Gorzel K, Murphy M. Mitochondrial dynamics, a new therapeutic target for triple negative breast Cancer. Biochim Biophys Acta BBA - Rev Cancer. 2021;1875:188518.
35. Torresano L, Nuevo-Tapioles C, Santacatterina F, Cuezva JM. Metabolic reprogramming and disease progression in cancer patients. Biochim Biophys Acta BBA-Mol Basis Dis. 2020;1866:165721.
36. Cui L, Gouw AM, LaGory EL, Guo S, Attarwala N, Tang Y, et al. Mitochondrial copper depletion suppresses triple-negative breast cancer in mice. Nat Biotechnol. 2021;39:357–67.
37. Humphries BA, Cutter AC, Buschhaus JM, Chen Y-C, Qyli T, Palagama DSW, et al. Enhanced mitochondrial fission suppresses signaling and metastasis in triple-negative breast cancer. Breast Cancer Res. 2020;22:60.
38. Hayes JD, Dinkova-Kostova AT, Tew KD. Oxidative stress in Cancer. Cancer Cell. 2020;38:167–97.
39. Kalpage HA, Wan J, Morse PT, Zurek MP, Turner AA, Khobeir A, et al. Cytochrome C phosphorylation: control of mitochondrial electron transport chain flux and apoptosis. Int J Biochem Cell Biol. 2020;121:105704.
40. Wan J, Zhang X, Li Z, Mo F, Tang D, Xiao H, et al. Oxidative stress amplifiers as Immunogenic cell death nanoinducers disrupting mitochondrial redox homeostasis for Cancer immunotherapy. Adv Healthc Mater. 2023;12:2202710.
41. Bao W, Liu M, Meng J, Liu S, Wang S, Jia R, et al. MOFs-based nanoagent enables dual mitochondrial damage in synergistic antitumor therapy via oxidative stress and calcium overload. Nat Commun. 2021;12:6399.
42. Lu L, Liu G, Lin C, Li K, He T, Zhang J, et al. Mitochondrial metabolism targeted nanoplatform for efficient Triple-Negative breast Cancer combination therapy. Adv Healthc Mater. 2021;10:2100978.
43. Chen C, Ni X, Jia S, Liang Y, Wu X, Kong D, et al. Massively evoking Immunogenic cell death by focused mitochondrial oxidative stress using an AIE luminogen with a twisted molecular structure. Adv Mater. 2019;31:1904914.
44. Gong N, Ma X, Ye X, Zhou Q, Chen X, Tan X, et al. Carbon-dot-supported atomically dispersed gold as a mitochondrial oxidative stress amplifier for cancer treatment. Nat Nanotechnol. 2019;14:379–87.
45. Bonekamp NA, Peter B, Hillen HS, Felser A, Bergbrede T, Choidas A, et al. Small-molecule inhibitors of human mitochondrial DNA transcription. Nature. 2020;588:712–6.
46. Vasan K, Werner M, Chandel NS. Mitochondrial metabolism as a target for Cancer therapy. Cell Metab. 2020;32:341–52.
47. Tsvetkov P, Detappe A, Cai K, Keys HR, Brune Z, Ying W, et al. Mitochondrial metabolism promotes adaptation to proteotoxic stress. Nat Chem Biol. 2019;15:681–9.
48. Lee J, Yesilkanal AE, Wynne JP, Frankenberger C, Liu J, Yan J, et al. Effective breast cancer combination therapy targeting BACH1 and mitochondrial metabolism. Nature. 2019;568:254–8.
49. Huang T, Zhang T, Gao J. Targeted mitochondrial delivery: A therapeutic new era for disease treatment. J Controlled Release. 2022;343:89–106.
50. Huang M, Myers CR, Wang Y, You M. Mitochondria as a novel target for Cancer chemoprevention: emergence of Mitochondrial-targeting agents. Cancer Prev Res (Phila Pa). 2021;14:285–306.
51. Cho H, Cho Y-Y, Shim MS, Lee JY, Lee HS, Kang HC. Mitochondria-targeted drug delivery in cancers. Biochim Biophys Acta BBA - Mol Basis Dis. 2020;1866:165808.
52. Wang R, Qiu M, Zhang L, Sui M, Xiao L, Yu Q, et al. Augmenting immunotherapy via bioinspired MOF-Based ROS homeostasis disruptor with Nanozyme-Cascade reaction. Adv Mater. 2023;35:202306748.
53. Pan Y, Liu Y, Zeng G, Zhao L, Lai Z. Rapid synthesis of zeolitic imidazolate framework-8 (ZIF-8) nanocrystals in an aqueous system. Chem Commun. 2011;47:2071.
54. Venna SR, Jasinski JB, Carreon MA. Structural evolution of zeolitic imidazolate Framework-8. J Am Chem Soc. 2010;132:18030–3.
55. Vuković L, Khatib FA, Drake SP, Madriaga A, Brandenburg KS, Král P, et al. Structure and dynamics of highly PEG-ylated sterically stabilized micelles in aqueous media. J Am Chem Soc. 2011;133:13481–8.
56. Zhang D, Teng K, Zhao L, Niu L, Yang Q. Ultra-Small Nano-Assemblies as Tumor-Targeted and renal clearable theranostic agent for photodynamic therapy. Adv Mater. 2023;35:202209789.
57. Wang H, Yu D, Fang J, Cao C, Liu Z, Ren J, et al. Renal-Clearable porphyrinic Metal-Organic framework nanodots for enhanced photodynamic therapy. ACS Nano. 2019;13:9206–17.
58. Zeng W, Wu X, Chen T, Sun S, Shi Z, Liu J, et al. Renal-Clearable ultrasmall polypyrrole nanoparticles with Size-Regulated property for second Near-Infrared Light-Mediated photothermal therapy. Adv Funct Mater. 2021;31:202008362.
59. Tian B, Liu S, Feng L, Liu S, Gai S, Dai Y, et al. Renal-Clearable Nickel-Doped carbon Dots with boosted photothermal conversion efficiency for multimodal Imaging-Guided Cancer therapy in the second Near-Infrared Biowindow. Adv Funct Mater. 2021;31:202100549.
60. Ma X, Huang Y, Chen W, Liu J, Liu SH, Yin J, et al. J-Aggregates formed by NaCl treatment of Aza-Coating heptamethine cyanines and their application to monitoring salt stress of plants and promoting photothermal therapy of tumors. Angew Chem Int Ed. 2023;62:202216109.
61. Sun C, Li B, Zhao M, Wang S, Lei Z, Lu L, et al. J-Aggregates of cyanine dye for NIR-II in vivo dynamic vascular imaging beyond 1500 Nm. J Am Chem Soc. 2019;141:19221–5.
62. Hecht M, Würthner F. Supramolecularly engineered J-Aggregates based on perylene bisimide dyes. Acc Chem Res. 2021;54:642–53.
63. Xu J, Zheng X, Ren T-B, Shi L, Yin X, Yuan L, et al. Recent advances in near-infrared-II organic J-aggregates for bio-applications. Coord Chem Rev. 2025;528:216379.
64. Sun C, Sun X, Pei P, He H, Ming J, Liu X, et al. NIR-II J-Aggregates labelled mesoporous implant for Imaging-Guided osteosynthesis with minimal invasion. Adv Funct Mater. 2021;31:202100656.
65. Xu S, Liu H-W, Huan S-Y, Yuan L, Zhang X-B. Recent progress in utilizing near-infrared J-aggregates for imaging and cancer therapy. Mater Chem Front. 2021;5:1076–89.
66. Xue J, Liang Q, Wang R, Hou J, Li W, Peng Q, et al. Highly efficient thermally activated delayed fluorescence via J-Aggregates with strong intermolecular charge transfer. Adv Mater. 2019;31:201808242.
67. Xi D, Xu N, Xia X, Shi C, Li X, Wang D, et al. Strong π–π stacking stabilized nanophotosensitizers: improving tumor retention for enhanced therapy for large tumors in mice. Adv Mater. 2022;34:202106797.
68. Feng W, Liu D, Feng S, Feng G. Readily available fluorescent probe for carbon monoxide imaging in living cells. Anal Chem. 2016;88:10648–53.
69. Ding L, Madamsetty VS, Kiers S, Alekhina O, Ugolkov A, Dube J, et al. Glycogen synthase Kinase-3 Inhibition sensitizes pancreatic Cancer cells to chemotherapy by abrogating the TopBP1/ATR-Mediated DNA damage response. Clin Cancer Res. 2019;25:6452–62.

70. Kleih M, Böpple K, Dong M, Gaißler A, Heine S, Olayioye MA, et al. Direct impact of cisplatin on mitochondria induces ROS production that dictates cell fate of ovarian cancer cells. Cell Death Dis. 2019;10:851.

Publisher's note